

Impact of Assimilating Microwave Radiances with a Limited-Area Ensemble Data Assimilation System on Forecasts of Typhoon Morakot

CRAIG S. SCHWARTZ AND ZHIQUAN LIU

National Center for Atmospheric Research, Boulder, Colorado

YONGSHENG CHEN

York University, Toronto, Ontario, Canada

XIANG-YU HUANG

National Center for Atmospheric Research, Boulder, Colorado

(Manuscript received 23 March 2011, in final form 18 October 2011)

ABSTRACT

Two parallel experiments were designed to evaluate whether assimilating microwave radiances with a cyclic, limited-area ensemble adjustment Kalman filter (EAKF) could improve track, intensity, and precipitation forecasts of Typhoon Morakot (2009). The experiments were configured identically, except that one assimilated microwave radiances and the other did not. Both experiments produced EAKF analyses every 6 h between 1800 UTC 3 August and 1200 UTC 9 August 2009, and the mean analyses initialized 72-h Weather Research and Forecasting model forecasts. Examination of individual forecasts and average error statistics revealed that assimilating microwave radiances ultimately resulted in better intensity forecasts compared to when radiances were withheld. However, radiance assimilation did not substantially impact track forecasts, and the impact on precipitation forecasts was mixed. Overall, net positive results suggest that assimilating microwave radiances with a limited-area EAKF system is beneficial for tropical cyclone prediction, but additional studies are needed.

1. Introduction

In the past ~20 yr, human forecasts of tropical cyclone (TC) tracks have improved substantially but intensity forecasts have improved little (Rappaport et al. 2009). However, advances in data assimilation (DA) techniques may lead to better forecasts of TC intensity and a continued reduction in track error.

One such advance concerns ensemble data assimilation (EnDA) techniques [such as the ensemble Kalman filter (Evensen 1994; Burgers et al. 1998; Houtekamer and Mitchell 1998)]. Although most operational centers currently use deterministic variational DA systems to initialize their forecast models, a number of studies have shown that employing EnDA techniques to initialize

numerical weather prediction (NWP) model forecasts produces better quality forecasts than those initialized with three-dimensional variational data assimilation (3DVAR) methods (e.g., Meng and Zhang 2008a,b; Szunyogh et al. 2008; Whitaker et al. 2008; Torn and Hakim 2009; Zhang et al. 2009, 2010; Torn 2010; Hamill et al. 2011, Zhang et al. 2011) and similar quality forecasts as those initialized with 4DVAR systems (e.g., Buehner et al. 2010a,b; Miyoshi et al. 2010; Zhang et al. 2011). In contrast to the static, isotropic background error covariances (BECs) typically used in 3DVAR systems (e.g., Parrish and Derber 1992), EnDA algorithms calculate flow-dependent BECs from an ensemble of short-term forecasts. TC initialization may particularly benefit from these ensemble-derived, flow-dependent BECs, as they are more likely to better represent mass–wind balances than static BECs.

Therefore, a number of EnDA studies have focused on TC prediction and demonstrated that NWP model forecasts initialized with EnDA systems are competitive

Corresponding author address: Craig S. Schwartz, National Center for Atmospheric Research, 3090 Center Green Drive, Boulder, CO 80301.

E-mail: schwartz@ucar.edu

with or better than operational numerical forecasts of TC track and intensity (e.g., Torn and Hakim 2009; Zhang et al. 2009, 2010; Torn 2010; Hamill et al. 2011). Moreover, sensitivity studies by Li and Liu (2009) and Liu and Li (2010) showed that EnDA of high-resolution (~ 15 -km) temperature and moisture profiles retrieved from infrared satellite soundings improved TC track and intensity forecasts compared to when they were not assimilated.

Based on the findings of Li and Liu (2009) and Liu and Li (2010), it appears that EnDA of satellite observations can improve NWP model forecasts of TCs. As there are few in situ observations over the ocean, EnDA of satellite-measured microwave radiances may also be useful for TC forecasting applications. Since microwave frequencies can penetrate nonprecipitating clouds, remote sensing at these frequencies consistently provides valuable observations over data-sparse regions. Many studies have shown that assimilating microwave radiances with variational DA algorithms improves forecasts, especially for midrange lead times in global models over areas with few conventional observations¹ (e.g., Caplan et al. 1997; Derber and Wu 1998; Simmons and Hollingsworth 2002; Zapotocny et al. 2007, 2008). Operationally, hundreds of thousands of microwave radiance observations are assimilated in global systems each day (e.g., Houtekamer et al. 2009).

Successfully assimilating microwave radiances requires a radiative transfer model (RTM), observation thinning, bias correction (e.g., Dee 2005), and careful vertical localization (e.g., Campbell et al. 2010). Implementing these features within an EnDA framework presents formidable challenges. Nonetheless, several studies have directly assimilated microwave radiances within global EnDA configurations (Houtekamer et al. 2005; Buehner et al. 2010a,b; Miyoshi et al. 2010; Hamill et al. 2011) and sensitivity analyses reported the radiances yielded positive impacts (Miyoshi and Sato 2007; Aravéquia et al. 2011). We note that some of these studies utilized an external variational DA system to bias correct the radiances (e.g., Houtekamer et al. 2005; Miyoshi and Sato 2007; Buehner et al. 2010b), while the EnDA systems described by Miyoshi et al. (2010) and Aravéquia et al. (2011) performed radiance bias correction completely within ensemble frameworks.

Despite many successful applications of EnDA techniques within limited-area models (reviewed in Meng and Zhang 2011), to our knowledge, microwave radiances have never been assimilated with a limited-area

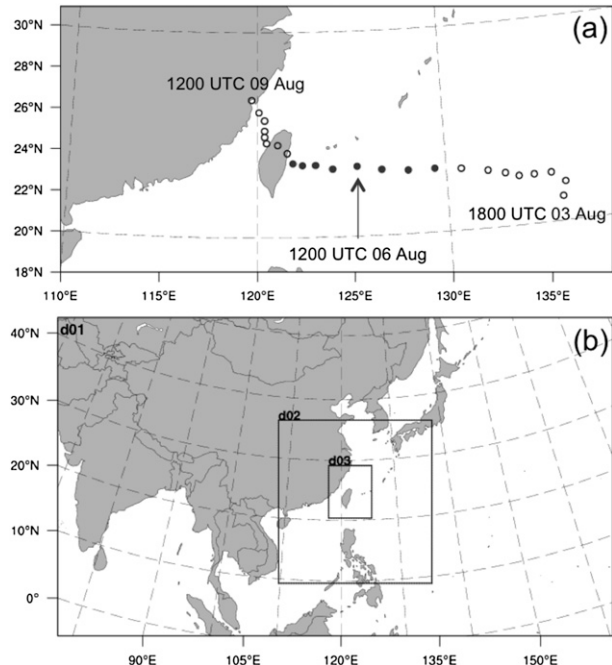


FIG. 1. (a) “Best track” of Typhoon Morakot provided by the JTWC and (b) computational domain used for all experiments. In (a) Morakot’s estimated center of circulation is plotted every 6 h beginning at 1800 UTC 3 Aug and ending at 1200 UTC 9 Aug. Filled (open) circles indicate Morakot was at typhoon (tropical storm or depression) strength.

EnDA system. It is important to understand how EnDA of radiances influences regional forecasts, as limited-area and global NWP systems may respond differently to radiance DA due to nonuniform satellite coverage in the former. Specifically, this nonuniform coverage makes bias correction of radiances more challenging than in a global model. Moreover, some regional studies using variational DA techniques have either suggested the forecast impact of radiance assimilation does not persist as long as in a global system (Zapotocny et al. 2005) or found an unclear overall impact (Xu et al. 2009), possibly due to lateral boundary condition (LBC) contamination (Warner et al. 1997).

Thus, to investigate this topic, this work assesses whether assimilating microwave radiances with a limited-area EnDA system can improve rainfall, track, and intensity forecasts of Typhoon Morakot (August 2009; Fig. 1a), which produced torrential precipitation over Taiwan and China (Zhang et al. 2010). Specifically, forecasts from the Advanced Research Weather Research and Forecasting Model (ARW-WRF; Skamarock et al. 2008) were initialized from ensemble adjustment Kalman filter (EAKF; Anderson 2001, 2003; Liu et al. 2007) analyses produced by software from the Data Assimilation Research Testbed (DART; Anderson et al. 2009).

¹ Herein, “conventional observations” means all observations other than microwave radiances.

An overview of Typhoon Morakot is provided in section 2, and model configurations and the experimental design are described in section 3. Results are presented in section 4 before concluding in section 5.

2. Overview of Typhoon Morakot

According to the Joint Typhoon Warning Center's (JTWC) "best track" analyses, Morakot became a tropical depression at 1800 UTC 3 August and was classified as a minimal tropical storm at 0600 UTC 4 August. The cyclone gradually strengthened as it was steered steadily westward (Fig. 1a) by high pressure to its north and east. Morakot intensified to a typhoon with 75-kt winds at 1800 UTC 5 August, where 1 knot (kt) = 0.514 m s^{-1} . Winds increased to a maximum of 80 kt by 0000 UTC 6 August and a minimum central pressure of 954 hPa was attained at 0000 UTC 7 August. Morakot was an extremely large system, and at its peak intensity, gale force winds extended more than 400 km from the center of circulation. The cyclone slowed as it approached Taiwan and made landfall as an 80-kt typhoon around 1800 UTC 7 August.

After landfall, Morakot weakened rapidly. The center emerged over the Taiwan Strait around 0600 UTC 8 August as a 45-kt tropical storm. The system then moved slowly north-northwest, remaining a minimal tropical storm until its second landfall in China around 1200 UTC 9 August. Long after the center departed Taiwan, southwesterly winds associated with the storm's circulation led to orographically enhanced precipitation over Taiwan, leading to devastating amounts of precipitation.

3. Model configurations and experimental design

Two parallel experiments using 64-member ensembles were configured to determine the effect of microwave radiance DA with a limited-area EAKF on numerical forecasts of Typhoon Morakot. The first experiment assimilated solely conventional observations, including surface, rawinsonde, aircraft, and satellite wind data, while the second also assimilated microwave radiances² from Advanced Microwave Sounding Units A and B (AMSU-A and -B) and Microwave Humidity Sounder (MHS) sensors outfitted on polar-orbiting satellites (Table 1). AMSU-A sensors have a resolution of $\sim 48 \text{ km}$ at nadir, while the AMSU-B and MHS sensors have resolutions of $\sim 16 \text{ km}$ at nadir. The raw radiances were thinned on

TABLE 1. Satellite IDs, sensors, and channels that were assimilated. AMSU-A channel 4 was assimilated over water only and AMSU-A channel 5 was only assimilated over points with model-predicted surface pressures greater than 850 hPa.

Satellite ID	Sensor	Channels
<i>NOAA-15</i>	AMSU-A	4–8
<i>NOAA-15</i>	AMSU-B	3, 5
<i>NOAA-18</i>	AMSU-A	4–8
<i>NOAA-18</i>	MHS	3–5
<i>METOP-2</i>	AMSU-A	4–6, 8
<i>METOP-2</i>	MHS	3–5

a 90-km grid and assimilated for nonprecipitating grid boxes only. AMSU-A channel 4 was only assimilated over water, and AMSU-A channel 5 was only assimilated over points with model-predicted surface pressures greater than 850 hPa. Radiance observations were rejected over pixels with mixed surface types (i.e., pixels containing both land and sea), and observations with scan angles greater than $\sim 41^\circ$ were not assimilated. Assimilating radiances most directly alters model temperature and moisture profiles, but radiances can also impact wind fields through multivariate BECs.

As polar-orbiting satellite positions vary temporally, data from a given satellite may have been unavailable over the computational domain at a particular analysis time. Nonetheless, an average of $\sim 25\,000$ radiances were assimilated each analysis cycle. Figure 2 shows the locations of radiances that were assimilated each analysis on 6 August and the best-track locations of Typhoon Morakot. Many radiances were assimilated around the cyclone on 6 August, and the satellite coverage was similar on other dates.

Aside from the difference in assimilated observations, the two experiments were otherwise configured identically, thus permitting a clear assessment of the impact of microwave radiance DA. For example, both experiments were integrated over the same triple-nested computational domain (Fig. 1b). Horizontal grid lengths in the outermost (d01), middle (d02), and innermost (d03) domains were 45, 15, and 5 km, respectively. The nests were linked via one-way nesting and the inner domains' forecasts were initialized from the 45-km analyses. There were 45 vertical levels and the model top was 30 hPa. Both experiments used the following parameterizations: the Goddard microphysics scheme (Tao and Simpson 1993; Tao et al. 2003), the Rapid Radiative Transfer Model (RRTM) longwave (Mlawer et al. 1997) and Goddard shortwave (Chou and Suarez 1994) radiation schemes, the Yonsei University (YSU) boundary layer scheme (Hong et al. 2006), the Noah land surface model (Chen and Dudhia 2001), and Grell–Devenyi cumulus parameterization (Grell and Devenyi 2002).

² Satellites sense radiation at known frequencies, so measured radiances can be converted to brightness temperatures by inverting the Planck function. Strictly speaking, we assimilated brightness temperatures rather than radiances.

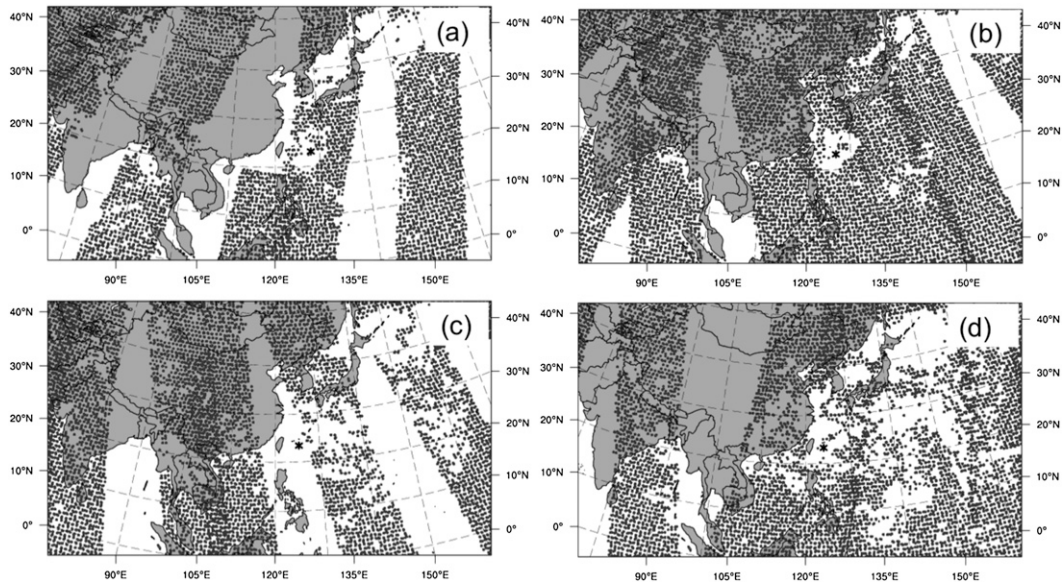


FIG. 2. Locations (dots) where at least one microwave radiance was assimilated during the (a) 0000, (b) 0600, (c) 1200, and (d) 1800 UTC analyses on 6 Aug. The best-track location of Morakot is denoted in each panel by an asterisk.

The parameterizations were identical across the nests, except that no cumulus parameterization was used in d03. The National Centers for Environmental Prediction's (NCEP) Global Forecast System (GFS) provided the LBCs, and neither experiment employed any cyclone relocation scheme nor assimilated TC position or intensity.

The DA procedures were also common among the experiments. Observations within ± 3 h of the analyses were assimilated only in the 45-km domain (d01). All observations were assumed to be valid at the analysis times. Horizontal covariance localization forced analysis increments to zero beyond ~ 1200 km from an observation location. Increments were also constrained vertically to within ~ 6 km of an observation. Similar to Hamill et al. (2011), observation operators from the ARW-WRF data assimilation (ARW-WRFDA, hereafter WRFDA; Barker et al. 2004) system generated the prior (before assimilation) model-simulated observations for each ensemble member.³ The Community Radiative Transfer Model (CRTM; Han et al. 2006) was coupled to the WRFDA system and used to calculate model-simulated brightness temperatures. The vertical location of each radiance was set to the model level at which its weighting function was maximized (as in Houtekamer et al. 2005; Hamill et al. 2011). Variational bias correction

(Derber and Wu 1998; Dee 2005; Auligné et al. 2007) of raw radiances was achieved by performing WRFDA-3DVAR analyses over the computational domain for a week-long period with full cycling to "spin up" bias correction coefficients. The spunup coefficients at the end of the week were used to bias correct the radiances for the duration of the EAKF experiment. Radiance bias correction during the EAKF experiment was performed within WRFDA-3DVAR using the spunup coefficients.

The initial ensemble was constructed by interpolating the 1200 UTC 3 August GFS analysis onto the model domain and adding random perturbations drawn from WRFDA-based BECs (see Torn et al. 2006). Perturbed LBCs for each analysis were generated in a similar manner. Then, the ARW-WRF generated an ensemble of 6-h forecasts that served as backgrounds for the first analysis (at 1800 UTC 3 August). This analysis initialized another set of 6-h ensemble forecasts to serve as backgrounds for the next analysis, and this 6-h cyclic forecast–analysis pattern continued until 1200 UTC 9 August. Additionally, a triple-nested 72-h ARW-WRF forecast was initialized from the ensemble mean analysis, each cycle beginning at 1800 UTC 4 August. The results from these 72-h forecasts are now described.

4. Results

Model predictions of Morakot's track, maximum wind speed (WS_{\max}), and minimum sea level pressure (SLP_{\min}) were verified against the JTWC's best-track analyses.

³ Hamill et al. (2011) used the Gridpoint Statistical Interpolation (GSI; Kleist et al. 2009) observation operators.

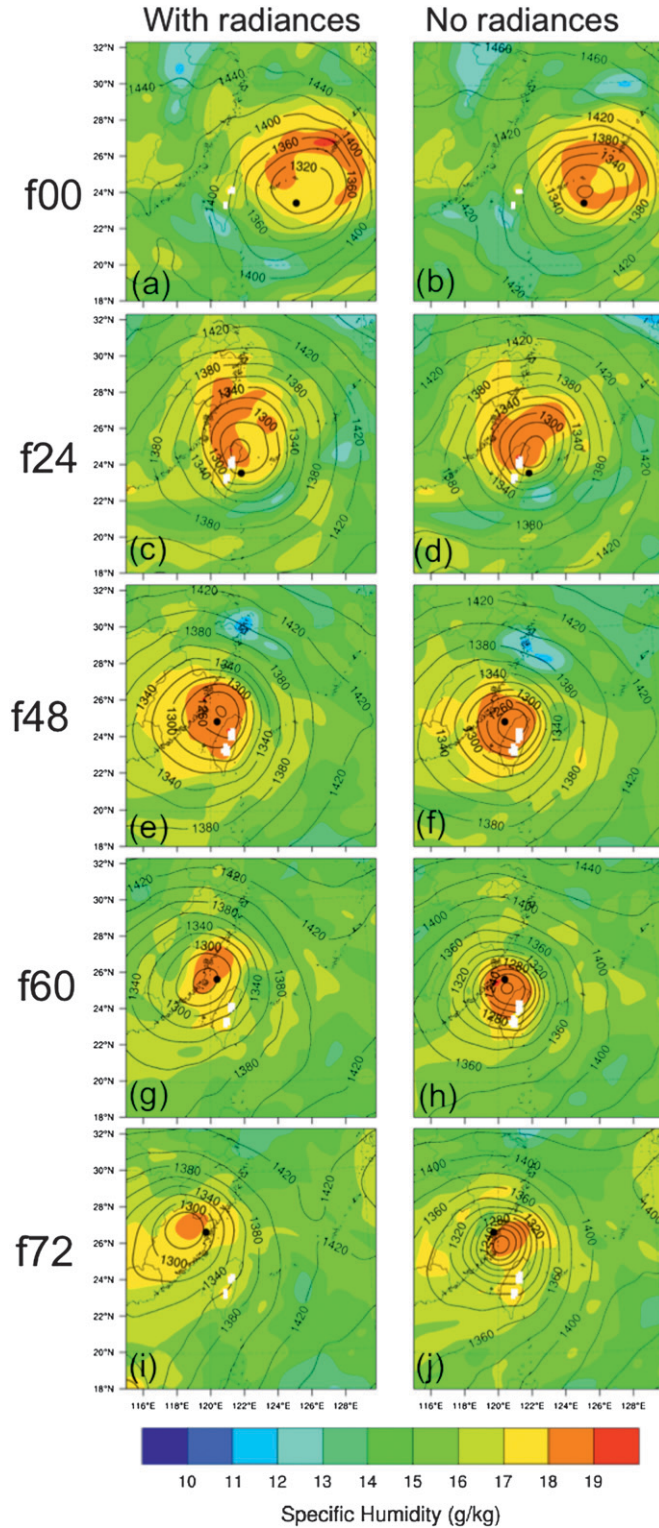


FIG. 3. The 850-hPa water vapor mixing ratio (g kg^{-1}) and height (contoured every 20 m) for (a),(b) 0-, (c),(d) 24-, (e),(f) 48-, (g),(h) 60-, and (i),(j) 72-h 15-km (d02) forecasts initialized from the 1200 UTC 6 Aug mean analyses for the experiments (left) with and (right) without radiances. The best-track locations of Morakot are marked by black dots. White shadings over Taiwan represent locations where the 850-hPa surface was underground.

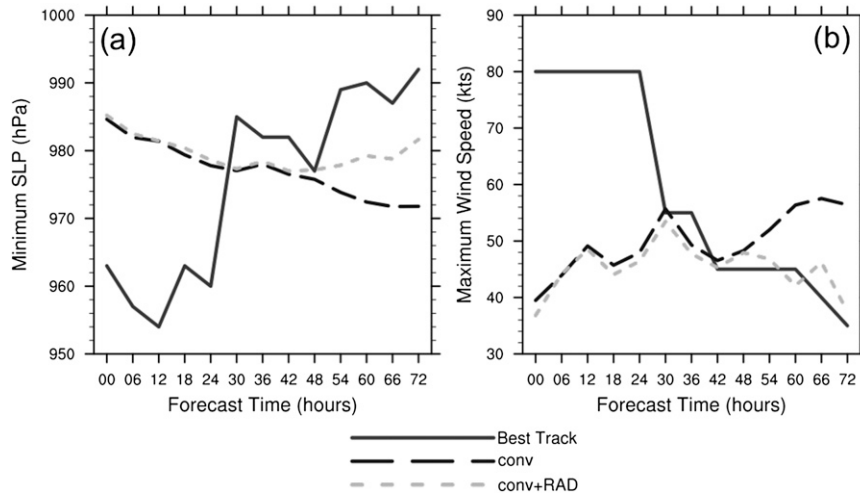


FIG. 4. The (a) SLP_{\min} (hPa) and (b) WS_{\max} (kt) model forecasts as a function of forecast hour calculated from the 15-km (d02) grids for the forecast initialized from the 1200 UTC 6 Aug mean analyses for the experiments with (conv+RAD) and without (conv) radiances. Also plotted are SLP_{\min} and WS_{\max} from the JTWC (best track).

Precipitation forecasts were compared to hourly rain-gauge data provided by the Taiwanese Central Weather Bureau (CWB). We first detail results for a single forecast before presenting statistics averaged over several initializations. Although DA was performed in the 45-km domain only, we primarily focus on results from the 15-km grid.

a. Single forecast

The 72-h forecast initialized after 12 DA cycles at 1200 UTC 6 August is now examined. Both mean 45-km analyses [interpolated onto the 15-km grid (d02; Figs. 3a,b)] predicted a TC in the western Pacific that captured Morakot's extremely large circulation. However, likely because of coarse grid spacing and the smoothing inherent in ensemble averaging, initial intensities were too weak (Fig. 4). Also, both experiments displaced the center slightly northward (Figs. 3a,b).

This northward bias persisted throughout the first 24 forecast hours (f24; Fig. 3c,d). Yet, the forward speed was forecasted quite well, as both experiments moved the system steadily westward to the northeastern coast of Taiwan by 1200 UTC 7 August (Figs. 3c,d) and then predicted slower motion (Figs. 3e-h). Intensity forecasts were similar through the first 30 forecast hours, with strengthening until landfall (\sim f30) followed by weakening upon interaction with Taiwan (Fig. 4).

However, after the TC entered the Taiwan Strait, substantial differences emerged. The experiment without radiances intensified the system, increasing WS_{\max} to almost 60 kt and decreasing SLP_{\min} markedly (Fig. 4). Conversely, the experiment with radiances weakened the

system, in agreement with the observations. The disparities in intensity were evident throughout the atmosphere, with warmer 500-hPa temperatures (Fig. 5) and deeper moisture (Figs. 3g,h) surrounding the TC in the experiment without radiances, indicative of a stronger system. As the experiment without radiances was too slow in bringing the cyclone onshore in China (Figs. 3i,j), the entire center of circulation remained over water for longer, which may have partially led to the intensification. But, land interaction cannot explain all of the differences, as the strengthening primarily occurred during a 12-h period (f48-f60; see Fig. 4) when both centers were over water. Since the only difference between the experiments was the addition of radiances, it appears that the cumulative impact of cyclic radiance DA led to initial conditions that better captured the overall environment in the vicinity of the TC and yielded an improved forecast. It is noteworthy that the influence of radiances at these later (f36-f72) forecast times was not masked by LBC contamination.

Finally, 5-km (d03) forecasts of accumulated precipitation over Taiwan were verified at sites where gauge data were available (Fig. 6). Both experiments produced 72-h precipitation amounts (Figs. 6a-c) exceeding 1 m over large portions of Taiwan. Excessive precipitation was predicted in north-central and northern Taiwan and the heavy rainfall over extreme southern Taiwan was not captured, likely because of the initial northward track bias. There was little difference regarding the experiments' general 72-h accumulated precipitation patterns, but the experiment without radiance DA produced a higher maximum, which is more consistent with the observations.

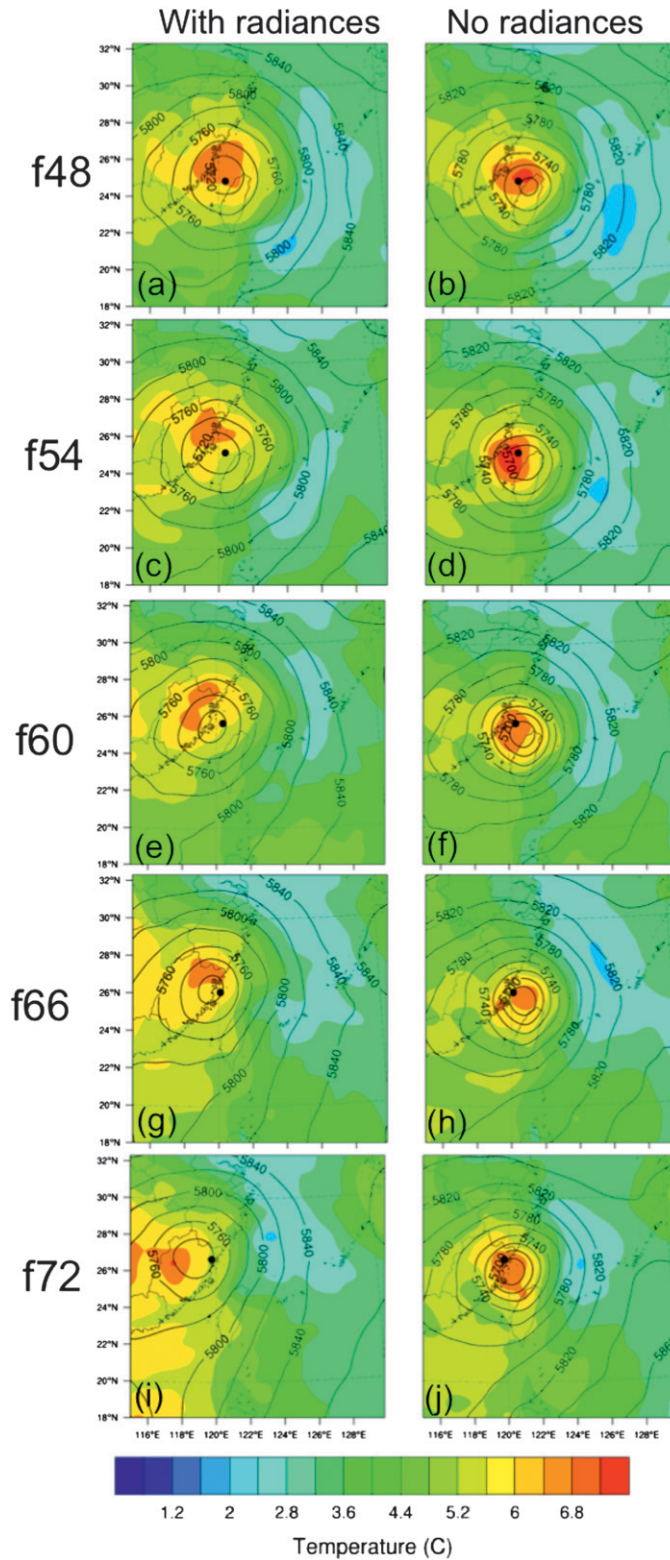


FIG. 5. The 500-hPa temperature ($^{\circ}\text{C}$) and height (contoured every 20 m) for (a),(b) 48-, (c),(d) 54-, (e),(f) 60-, (g),(h) 66-, and (i),(j) 72-h 15-km (d02) forecasts initialized from the 1200 UTC 6 Aug mean analyses for the experiments (left) with and (right) without radiances. The best-track locations of Morakot are marked by black dots.

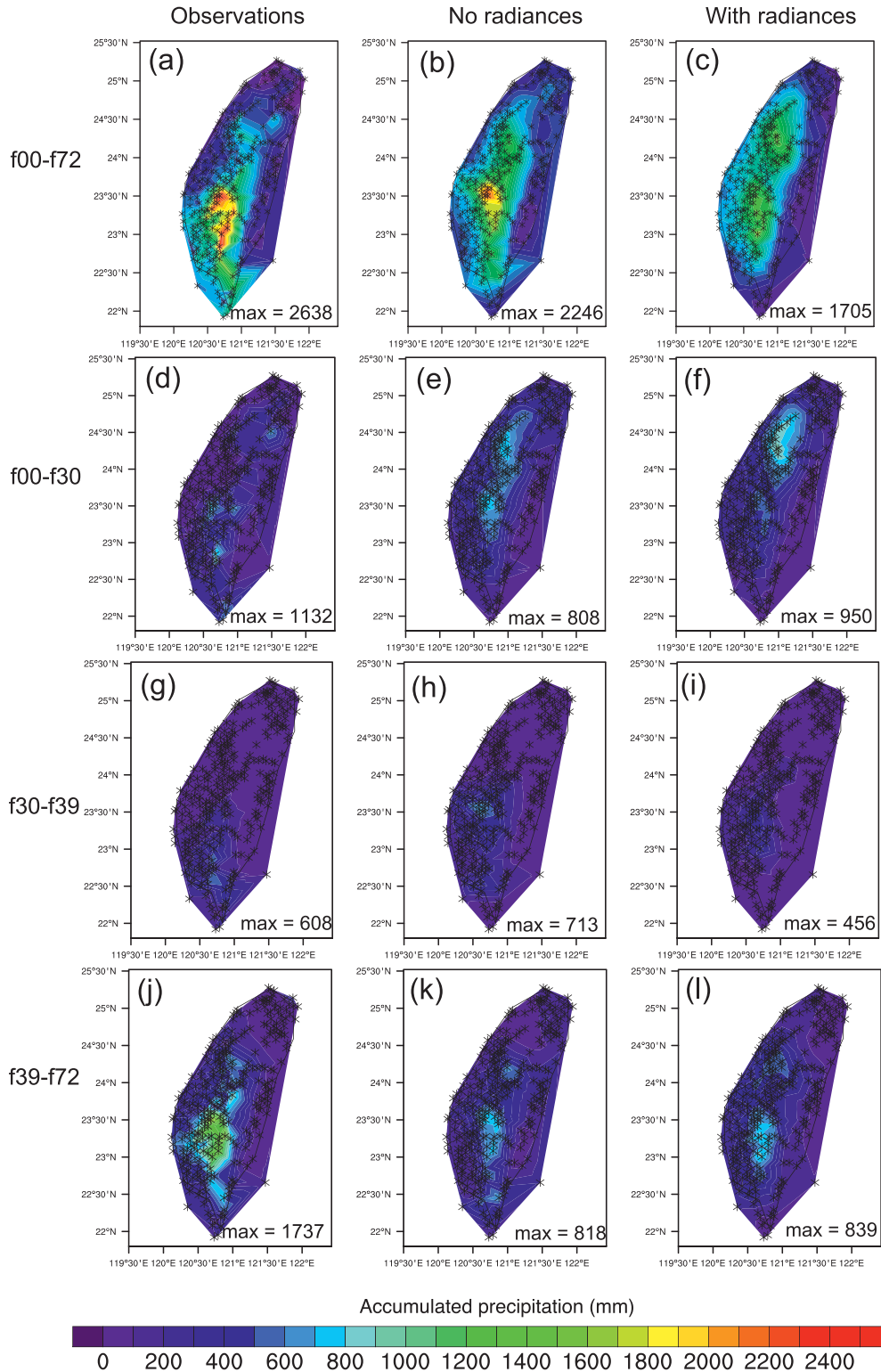


FIG. 6. (a) Observed 72-h accumulated precipitation between 1200 UTC 6 Aug and 1200 UTC 9 Aug and the corresponding 5-km (d03) forecasts from the experiments (b) without and (c) with radiances calculated at the locations where gauge data were available (asterisks). The other rows are as in (a)–(c), except they show observed and forecast (d)–(f) 30-h accumulated precipitation between 1200 UTC 6 Aug and 1800 UTC 7 Aug (f00–f30), (g)–(i) 9-h accumulated precipitation between 1800 UTC 7 Aug and 0300 UTC 8 Aug (f30–f39), and (j)–(l) 33-h accumulated precipitation between 0300 UTC 8 Aug and 1200 UTC 9 Aug (f39–f72).

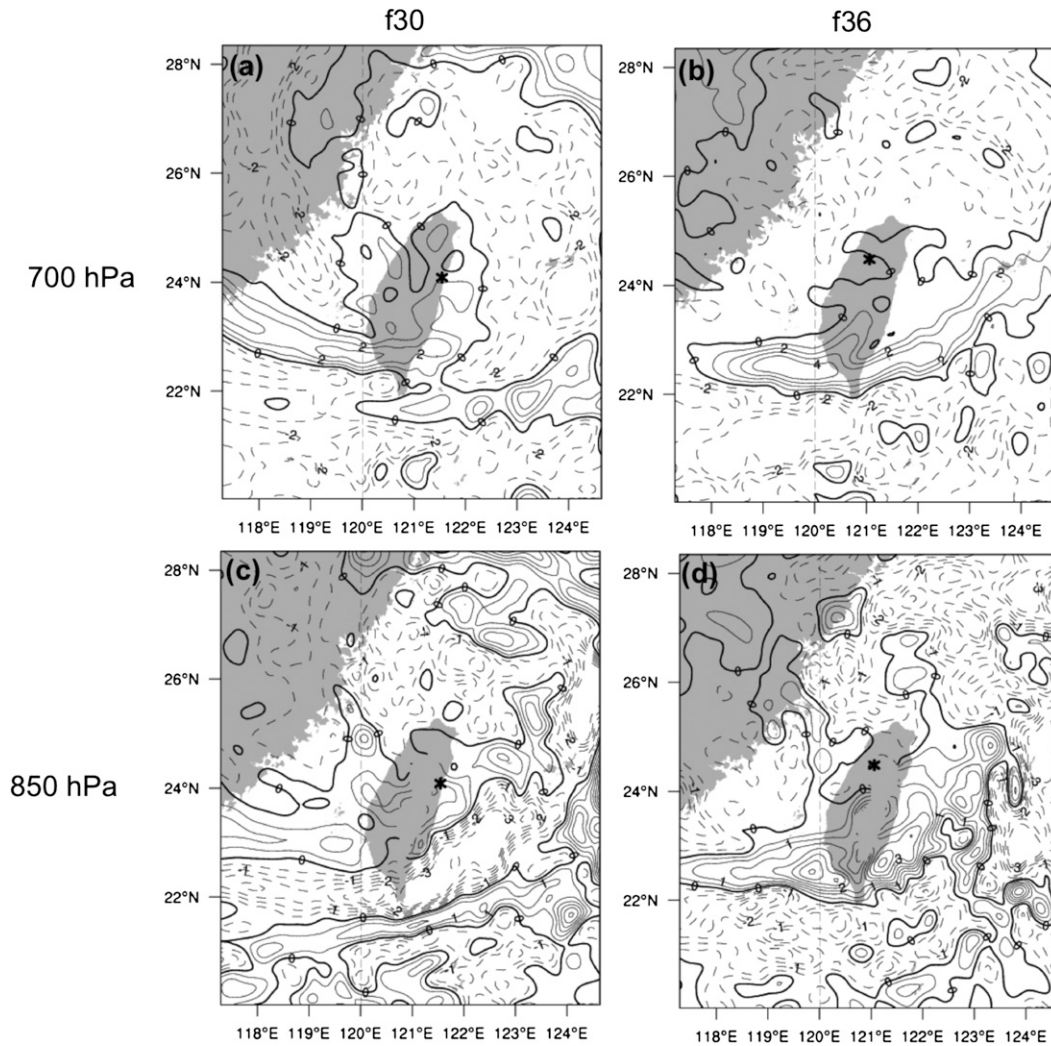


FIG. 7. Differences in the 5-km (d03) (a),(b) 700- and (c),(d) 850-hPa water vapor mixing ratio fields (g kg^{-1}) for the 30- and 36-h forecasts valid at (left) 1800 UTC 7 Aug and (right) 0000 UTC 8 Aug. The differences were calculated by subtracting output from the experiment with radiance DA from that of the experiment that did not assimilate radiances. Positive (negative) differences are denoted by solid (dashed) contours. Asterisks denote the best-track locations of Morakot, and the contour interval is 1.0 g kg^{-1} (0.5 g kg^{-1}) for the 700-hPa (850 hPa) difference fields. Broken contours over Taiwan in (c) and (d) indicate the 850-hPa surface was underground.

This disparity can be explained by partitioning the 72-h accumulated precipitation into three subperiods (Figs. 6d–l). The rainfall during the first 30 forecast hours (f00–f30; Figs. 6d–f) was quite similar between the experiments. Both produced heavy rainfall over portions of Taiwan in accordance with the observations but overpredicted precipitation over western and northern areas and missed the observed peak around 23°N . Bigger differences emerged regarding 9-h accumulated rainfall between 1800 UTC 7 August and 0300 UTC 8 August (f30–f39; Figs. 6g–i). During this period, the experiment without radiance DA produced substantially more precipitation than the experiment that assimilated radiances,

with a 9-h maximum of $\sim 700 \text{ mm}$. However, this maximum was displaced northward, and, overall, the experiment without radiance DA generated excessive rainfall. On the other hand, the experiment that assimilated radiances produced too little rainfall, but also placed the precipitation too far north. Difference fields (output from the experiment with radiance DA was subtracted from that of the experiment without radiance DA) of the 5-km (d03) 700- and 850-hPa water vapor mixing ratios (Fig. 7) reveal that the experiment without radiance DA was moister west of Taiwan during this time frame. This additional moisture likely contributed to the higher precipitation amounts in the

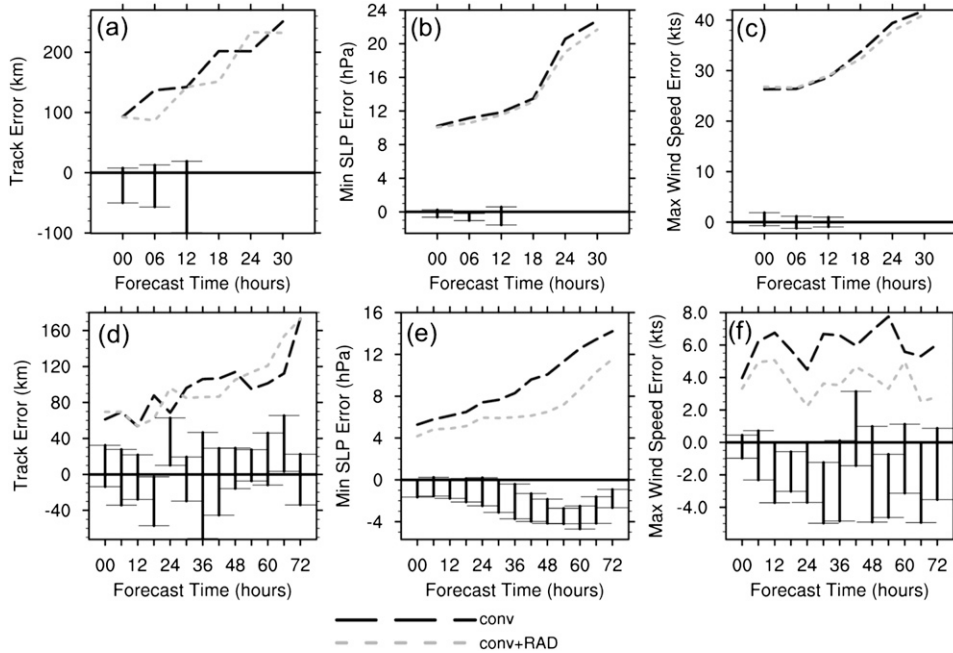


FIG. 8. (a) Average track error (km), (b) SLP_{min} error (hPa), and (c) WS_{max} error (kt) as a function of forecast hour for the strengthening phase (see text). (d)–(f) As in (a)–(c), but for the weakening phase. Bounds of the 90% confidence interval based upon differences between the two experiments’ errors (see text) are also shown. There were eight samples for each forecast hour during the weakening period, while during the strengthening phase, there were six samples at f00, and the number of samples decreased by one each successive lead time along the x axis. All statistics were calculated from the 15-km (d02) grids for the experiments with (conv+RAD) and without (conv) radiances.

experiment without radiance DA, as a westerly wind component transported the greater moisture onshore. Moreover, the advection of this enhanced moisture into the simulated TC may have contributed to the spurious intensification noted between f48–f72 in the experiment without radiance DA.

In the final 33 forecast hours (f39–f72; Figs. 6j–l), both experiments produced too little rainfall but placed the maximum in approximately the right location. The experiment that assimilated radiances better predicted the heavy rainfall on the western coast, and both experiments hinted at the observed secondary maximum around 24°N.

As a whole, despite the f30–f39 period, which caused the greater 72-h total rainfall in the experiment without radiance DA, precipitation amounts and patterns were quite similar between the two experiments. While there were shortcomings in both experiments, it is nonetheless impressive that they replicated the extreme precipitation event, and their forecasts were consistent with those in Zhang et al. (2010).

Many of the behaviors noted in this forecast were also observed with other initializations and are reflected in average statistics, which are now detailed.

b. Average results

Average 15-km (d02) error statistics were computed separately for Morakot’s “strengthening” (1800 UTC 4 August–0000 UTC 6 August; Figs. 8a–c) and “weakening” (1800 UTC 7 August–1200 UTC 9 August; Figs. 8d–f) phases. All forecasts with lead times *valid* during these periods were considered when determining statistics for a specific forecast hour (e.g., 72- and 6-h forecasts initialized at 1800 UTC 4 August fell into the weakening and strengthening phases, respectively). Statistical significance was assessed by applying a bootstrap resampling technique. Specifically, the difference between the experiments’ errors was calculated for each forecast. Random samples (with replacement) were drawn from the distribution of differences for each forecast hour with at least four samples, and the mean difference was calculated. This process was repeated 20 000 times. The 90% confidence interval for the average difference between the two experiments was estimated from the distribution of the resampled mean differences. If zero was not contained within the bounds of the confidence interval, then the difference between the experiments’ errors was statistically significant at the 95% level.

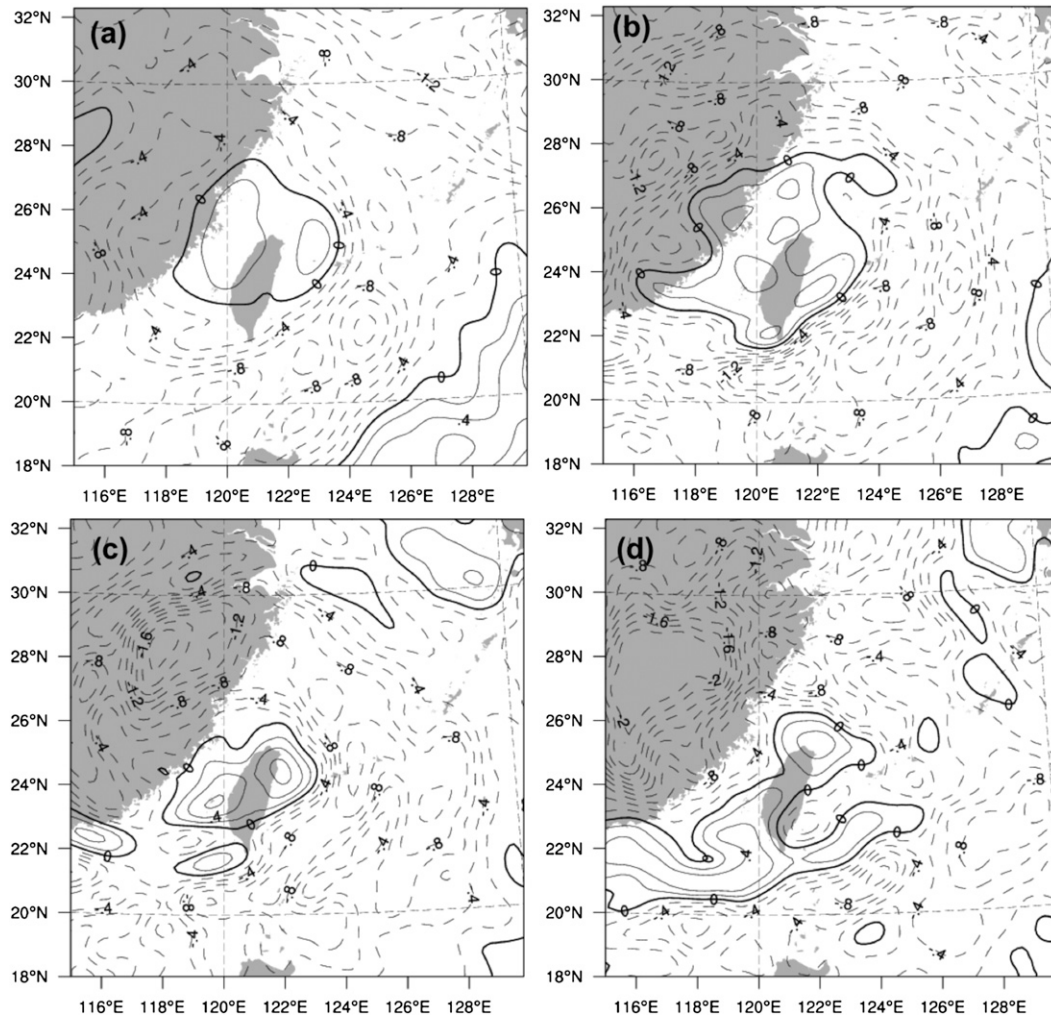


FIG. 9. Differences in the 15-km (d02) 700-hPa water vapor mixing ratio fields (g kg^{-1} ; contoured every 0.2 g kg^{-1}) aggregated over all (a) 0-, (b) 24-, (c) 48-, and (d) 72-h forecasts valid during Morakot's weakening phase. The differences were calculated by subtracting output from the experiment with radiance DA from that of the experiment that did not assimilate radiances. Positive (negative) differences are denoted by solid (dashed) contours.

For both phases, on average, neither experiment produced track forecasts superior to the other (Figs. 8a,d). During the strengthening period, radiances led to slightly lower SLP_{\min} and WS_{\max} errors (defined as the absolute difference between model-simulated and best-track values) between f18 and f30 (Figs. 8b,c), but the differences between the experiments were not clearly statistically significant. However, similar to the forecast initialized at 1200 UTC 6 August, more differences occurred during the weakening phase, where the experiment that assimilated radiances yielded forecasts with smaller SLP_{\min} and WS_{\max} errors (Figs. 8e,f) for all forecast hours. The differences between the two experiments were statistically significant at the 95% level for mean SLP_{\min} errors between f36 and f72 and nearly significant at earlier forecast hours. The average

WS_{\max} errors differed with 95% confidence at f12, f18, f30, f54, and f66. Most of the disparity regarding intensity errors during the weakening phase was due to the experiment without radiances incorrectly maintaining or increasing TC strength after the center of circulation entered the Taiwan Strait.

Forecasts valid during the weakening phase were further analyzed to explore thermodynamic differences between the two experiments. For a specific forecast hour, f (i.e., $f = 60$; 60-h forecasts), difference fields (calculated as in Fig. 7) were averaged over all f -hour forecasts valid during Morakot's weakening period. On average, the experiment without radiance DA was moister at 700 hPa (Fig. 9) around Taiwan at all forecast times, especially f48 (Fig. 9c). The same patterns were also evident at 850 and 500 hPa (not shown). Additionally, 500-hPa potential

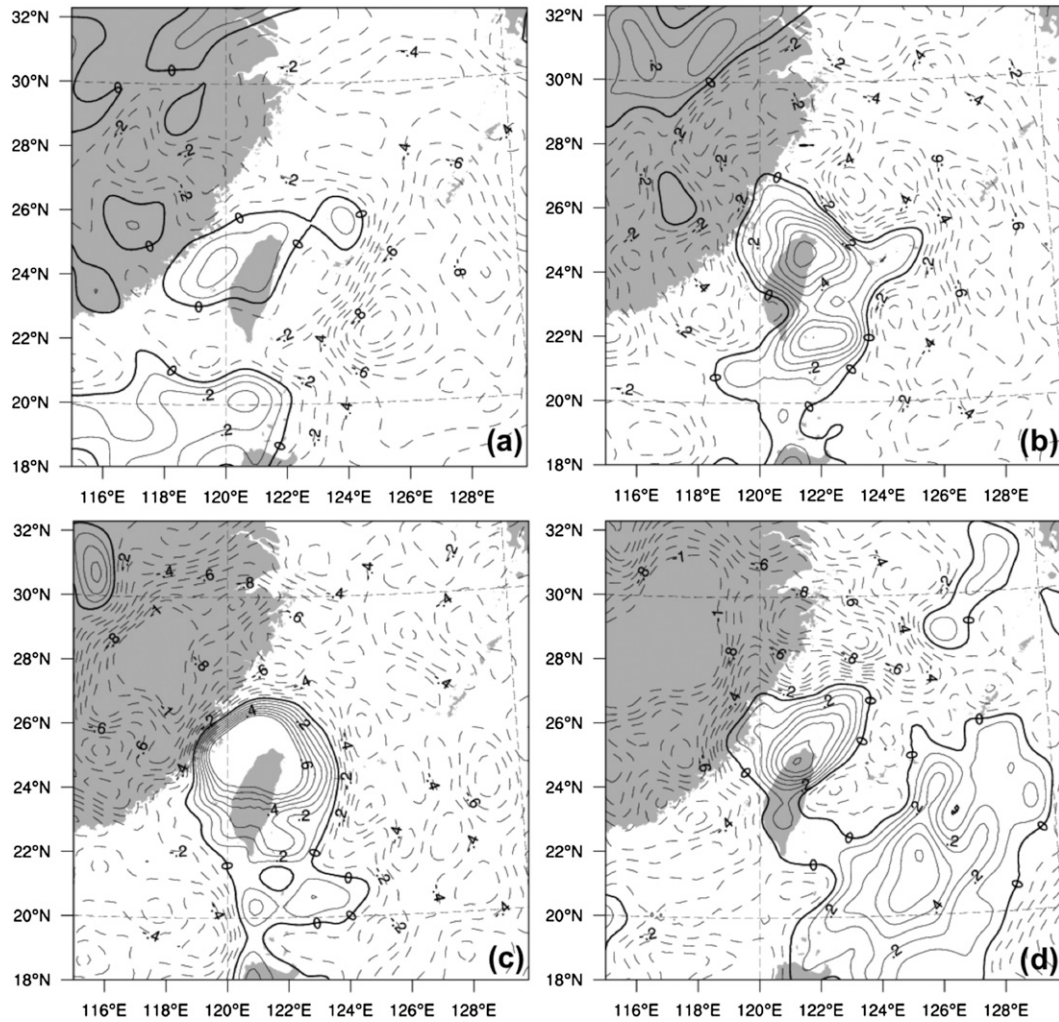


FIG. 10. As in Fig. 9, but here 500-hPa potential temperature differences (contoured every 0.1 K) are plotted.

temperature (Fig. 10) was generally warmer around Taiwan in the experiment without radiance DA, with similar patterns at 850, 700, and 300 hPa (not shown). The average warmer mid- and upper-level temperatures and moister conditions in the experiment without radiance DA reflect the stronger TCs predicted by that experiment. Conversely, the comparatively cooler, drier conditions in the experiment with radiance DA are consistent with the weaker TCs. As the only difference between the experiments was the addition of radiances, these thermodynamic differences can be solely attributed to the assimilation of microwave radiances.

5. Summary and conclusions

Two parallel experiments were designed to evaluate whether assimilating microwave radiances with a limited-area EAKF could improve track, intensity,

and precipitation forecasts of Typhoon Morakot. One experiment assimilated just conventional observations while the second also assimilated microwave radiances. Analyses were performed every 6 h between 1800 UTC 3 August and 1200 UTC 9 August, and beginning 1800 UTC 4 August, each mean analysis initialized a new 72-h ARW-WRF forecast.

On average, assimilating radiances produced better forecasts of SLP_{min} and WS_{max} , especially for 36–72-h forecasts during Morakot's weakening phase. However, radiance DA did not meaningfully improve intensity forecasts during the strengthening phase or alter track predictions, and the impact on precipitation forecasts was mixed. Overall, it appears that assimilating microwave radiances in addition to conventional observations within a limited-area EAKF framework is helpful for improving model forecasts of TC intensity. Since radiances were not assimilated near the core of model simulations of

Morakot (due to precipitation), radiance observations primarily modified large-scale initial conditions surrounding the modeled storms. Evidently, assimilating radiances resulted in model environmental fields that led to evolutions of simulated TCs that were more consistent with observations of Typhoon Morakot.

As we focused on a single weather event, we caution that additional studies over longer time periods and in a variety of weather regimes are needed to fully assess the impact of limited-area EnDA-based microwave radiance assimilation. Additionally, application of more sophisticated vertical localization techniques (e.g., Miyoshi and Sato 2007; Campbell et al. 2010) within regional domains warrants further attention and may realize additional value from assimilating radiances. Moreover, performing radiance bias correction fully within the ensemble framework [as in Miyoshi et al. (2010) and Aravéquia et al. (2011)] would enhance the practical applicability of our system. Finally, interpolation of the background fields to the observation times [as in Whitaker et al. (2008), Houtekamer et al. (2009), and Aravéquia et al. (2011)] may have yielded a larger impact from assimilating radiances.

Nevertheless, these promising results suggest initializing limited-area models with EnDA systems that assimilate microwave radiances is beneficial. Additional studies employing radiance DA in limited-area settings are planned and encouraged.

Acknowledgments. We are grateful to the United States Air Force Weather Agency for partially funding this work. Thanks to Ling-Feng Hsiao (Taiwan CWB) for providing precipitation data and Hui-Chuan Lin (NCAR) for assisting with radiance data processing. Comments from three anonymous reviewers helped improve this paper. NCAR is sponsored by the National Science Foundation.

REFERENCES

- Anderson, J. L., 2001: An ensemble adjustment Kalman filter for data assimilation. *Mon. Wea. Rev.*, **129**, 2884–2903.
- , 2003: A local least squares framework for ensemble filtering. *Mon. Wea. Rev.*, **131**, 634–642.
- , T. Hoar, K. Raeder, H. Liu, N. Collins, R. Torn, and A. Arellano, 2009: The Data Assimilation Research Testbed: A community facility. *Bull. Amer. Meteor. Soc.*, **90**, 1283–1296.
- Aravéquia, J. A., I. Szunyogh, E. J. Fertig, E. Kalnay, D. Kuhl, and E. J. Kostelich, 2011: Evaluation of a strategy for the assimilation of satellite radiance observations with the local-ensemble transform Kalman filter. *Mon. Wea. Rev.*, **139**, 1932–1951.
- Auligné, T., A. P. McNally, and D. P. Dee, 2007: Adaptive bias correction for satellite data in a numerical weather prediction system. *Quart. J. Roy. Meteor. Soc.*, **133**, 631–642.
- Barker, D. M., W. Huang, Y.-R. Guo, A. Bourgeois, and X. N. Xio, 2004: A three-dimensional variational data assimilation system for MM5: Implementation and initial results. *Mon. Wea. Rev.*, **132**, 897–914.
- Buehner, M., P. L. Houtekamer, C. Charette, H. L. Mitchell, and B. He, 2010a: Intercomparison of variational data assimilation and the ensemble Kalman filter for global deterministic NWP. Part I: Description and single-observation experiments. *Mon. Wea. Rev.*, **138**, 1550–1566.
- , —, —, —, and —, 2010b: Intercomparison of variational data assimilation and the ensemble Kalman filter for global deterministic NWP. Part II: One-month experiments with real observations. *Mon. Wea. Rev.*, **138**, 1567–1586.
- Burgers, G., P. J. van Leeuwen, and G. Evensen, 1998: Analysis scheme in the ensemble Kalman filter. *Mon. Wea. Rev.*, **126**, 1719–1724.
- Campbell, W. F., C. H. Bishop, and D. Hodyss, 2010: Vertical covariance localization for satellite radiances in ensemble Kalman filters. *Mon. Wea. Rev.*, **138**, 282–290.
- Caplan, P., J. Derber, W. Gemmill, S. Y. Hong, H. L. Pan, and D. Parish, 1997: Changes to the 1995 NCEP operational medium-range forecast model analysis–forecast system. *Wea. Forecasting*, **12**, 581–594.
- Chen, F., and J. Dudhia, 2001: Coupling an advanced land surface–hydrology model with the Penn State–NCAR MM5 modeling system. Part I: Model implementation and sensitivity. *Mon. Wea. Rev.*, **129**, 569–585.
- Chou, M.-D., and M. J. Suarez, 1994: An efficient thermal infrared radiation parameterization for use in general circulation models. NASA Tech. Memo. 104606, Vol. 3, 85 pp.
- Dee, D. P., 2005: Bias and data assimilation. *Quart. J. Roy. Meteor. Soc.*, **131**, 3323–3343.
- Derber, J. C., and W.-S. Wu, 1998: The use of TOVS cloud-cleared radiances in the NCEP SSI analysis system. *Mon. Wea. Rev.*, **126**, 2287–2299.
- Evensen, G., 1994: Sequential data assimilation with a nonlinear quasi-geostrophic model using Monte Carlo methods to forecast error statistics. *J. Geophys. Res.*, **99**, 10 143–10 162.
- Grell, G. A., and D. Devenyi, 2002: A generalized approach to parameterizing convection combining ensemble and data assimilation techniques. *Geophys. Res. Lett.*, **29**, 1693, doi:10.1029/2002GL015311.
- Hamill, T. M., J. S. Whitaker, M. Fiorino, and S. G. Benjamin, 2011: Global ensemble predictions of 2009’s tropical cyclones initialized with an ensemble Kalman filter. *Mon. Wea. Rev.*, **139**, 668–688.
- Han, Y., P. van Delst, Q. Liu, F. Weng, B. Yan, R. Treadon, and J. Derber, 2006: JCSDA Community Radiative Transfer Model (CRTM)—Version 1. NOAA Tech. Rep. NESDIS 122, 33 pp.
- Hong, S.-Y., Y. Noh, and J. Dudhia, 2006: A new vertical diffusion package with an explicit treatment of entrainment processes. *Mon. Wea. Rev.*, **134**, 2318–2341.
- Houtekamer, P. L., and H. L. Mitchell, 1998: Data assimilation using an ensemble Kalman filter technique. *Mon. Wea. Rev.*, **126**, 796–811.
- , —, G. Pellerin, M. Buehner, M. Charron, L. Spacek, and B. Hansen, 2005: Atmospheric data assimilation with an ensemble Kalman filter: Results with real observations. *Mon. Wea. Rev.*, **133**, 604–620.
- , —, and X. Deng, 2009: Model error representation in an operational ensemble Kalman filter. *Mon. Wea. Rev.*, **137**, 2126–2143.

- Kleist, D. T., D. F. Parrish, J. C. Derber, R. Treadon, W.-S. Wu, and S. Lord, 2009: Introduction of the GSI into the NCEP Global Data Assimilation System. *Wea. Forecasting*, **24**, 1691–1705.
- Li, J., and H. Liu, 2009: Improved hurricane track and intensity forecast using single field-of-view advanced IR sounding measurements. *Geophys. Res. Lett.*, **36**, L11813, doi:10.1029/2009GL038285.
- Liu, H., and J. Li, 2010: An improvement in forecasting rapid intensification of Typhoon Sinlaku (2008) using clear-sky full spatial resolution advanced IR soundings. *J. Appl. Meteor. Climatol.*, **49**, 821–827.
- , J. Anderson, Y.-H. Kuo, and K. Raeder, 2007: Importance of forecast error multivariate correlations in idealized assimilation of GPS radio occultation data with the ensemble adjustment filter. *Mon. Wea. Rev.*, **135**, 173–185.
- Meng, Z., and F. Zhang, 2008a: Tests of an ensemble Kalman filter for mesoscale and regional-scale data assimilation. Part III: Comparison with 3DVAR in a real-data case study. *Mon. Wea. Rev.*, **136**, 522–540.
- , and —, 2008b: Test of an ensemble Kalman filter for mesoscale and regional-scale data assimilation. Part IV: Comparison with 3DVAR in a month-long experiment. *Mon. Wea. Rev.*, **136**, 3671–3682.
- , and —, 2011: Limited-area ensemble-based data assimilation. *Mon. Wea. Rev.*, **139**, 2025–2045.
- Miyoshi, T., and Y. Sato, 2007: Assimilating satellite radiances with a local ensemble transform Kalman filter (LETKF) applied to the JMA global model (GSM). *SOLA*, **3**, 37–40.
- , —, and T. Kadowaki, 2010: Ensemble Kalman filter and 4D-Var intercomparison with the Japanese operational global analysis and prediction system. *Mon. Wea. Rev.*, **138**, 2846–2866.
- Mlawer, E. J., S. J. Taubman, P. D. Brown, M. J. Iacono, and S. A. Clough, 1997: Radiative transfer for inhomogeneous atmosphere: RRTM, a validated correlated- k model for the longwave. *J. Geophys. Res.*, **102**, 16 663–16 682.
- Parrish, D. F., and J. C. Derber, 1992: The National Meteorological Center's spectral statistical interpolation analysis system. *Mon. Wea. Rev.*, **120**, 1747–1763.
- Rappaport, E. N., and Coauthors, 2009: Advances and challenges at the National Hurricane Center. *Wea. Forecasting*, **24**, 395–419.
- Simmons, A. J., and A. Hollingsworth, 2002: Some aspects of the improvement in skill of numerical weather prediction. *Quart. J. Roy. Meteor. Soc.*, **128**, 647–677.
- Skamarock, W. C., and Coauthors, 2008: A description of the Advanced Research WRF, version 3. NCAR Tech. Note NCAR/TN-475+STR, 113 pp. [Available from UCAR Communications, P.O. Box 3000, Boulder, CO 80307.]
- Szunyogh, I., E. J. Kostelich, G. Gyarmati, E. Kalnay, B. R. Hunt, E. Ott, E. Satterfield, and J. A. Yorke, 2008: A local ensemble transform Kalman filter data assimilation system for the NCEP global model. *Tellus*, **60**, 113–130.
- Tao, W.-K., and J. Simpson, 1993: The Goddard Cumulus Ensemble model. Part I: Model description. *Terr. Atmos. Oceanic Sci.*, **4**, 35–72.
- , and Coauthors, 2003: Microphysics, radiation and surface processes in the Goddard Cumulus Ensemble (GCE) model. *Meteor. Atmos. Phys.*, **82**, 97–137.
- Torn, R. D., 2010: Performance of a mesoscale ensemble Kalman filter (EnKF) during the NOAA high-resolution hurricane test. *Mon. Wea. Rev.*, **138**, 4375–4392.
- , and G. J. Hakim, 2009: Ensemble data assimilation applied to RAINEX observations of Hurricane Katrina (2005). *Mon. Wea. Rev.*, **137**, 2817–2829.
- , —, and C. Snyder, 2006: Boundary conditions for limited-area ensemble Kalman filters. *Mon. Wea. Rev.*, **134**, 2490–2502.
- Warner, T. T., R. A. Peterson, and R. E. Treadon, 1997: A tutorial on lateral boundary conditions as a basic and potentially serious limitation to regional numerical weather prediction. *Bull. Amer. Meteor. Soc.*, **78**, 2599–2617.
- Whitaker, J. S., T. M. Hamill, X. Wei, Y. Song, and Z. Toth, 2008: Ensemble data assimilation with the NCEP Global Forecast System. *Mon. Wea. Rev.*, **136**, 463–482.
- Xu, J., S. Rugg, L. Byerle, and Z. Liu, 2009: Weather forecasts by the WRF-ARW model with the GSI data assimilation system in the complex terrain areas of southwest Asia. *Wea. Forecasting*, **24**, 987–1008.
- Zapotocny, T. H., W. P. Menzel, J. A. Jung, and J. P. Nelson III, 2005: A four-season impact study of rawinsonde, GOES, and POES data in the Eta Data Assimilation System. Part II: Contribution of the components. *Wea. Forecasting*, **20**, 178–198.
- , J. A. Jung, J. F. Le Marshall, and R. E. Treadon, 2007: A two-season impact study of satellite and in situ data in the NCEP Global Data Assimilation System. *Wea. Forecasting*, **22**, 887–909.
- , —, —, and —, 2008: A two-season impact study of four satellite data types and rawinsonde data in the NCEP Global Data Assimilation System. *Wea. Forecasting*, **23**, 80–100.
- Zhang, F., Y. Weng, J. A. Sippel, Z. Meng, and C. H. Bishop, 2009: Cloud-resolving hurricane initialization and prediction through assimilation of Doppler radar observations with an ensemble Kalman filter. *Mon. Wea. Rev.*, **137**, 2105–2125.
- , —, Y.-H. Kuo, J. S. Whitaker, and B. Xie, 2010: Predicting Typhoon Morakot's catastrophic rainfall with a convection-permitting mesoscale ensemble system. *Wea. Forecasting*, **25**, 1816–1825.
- Zhang, M., F. Zhang, X.-Y. Huang, and X. Zhang, 2011: Intercomparison of an ensemble Kalman filter with three- and four-dimensional variational data assimilation methods in a limited-area model over the month of June 2003. *Mon. Wea. Rev.*, **139**, 566–572.